



Efficient quasi-mesoscopic perovskite solar cells using Li-doped hierarchical TiO₂ as scaffold of scattered distribution



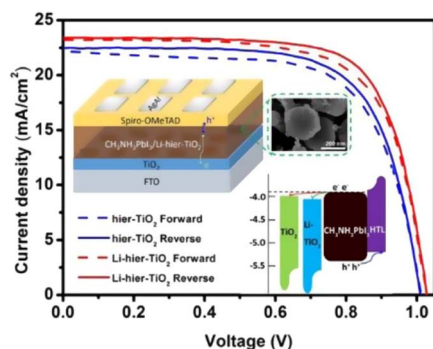
Xian Hou^a, Jianping Zhou^b, Sumei Huang^a, Wei Ou-Yang^a, Likun Pan^c, Xiaohong Chen^{a,*}

^a Engineering Research Center for Nanophotonics & Advanced Instrument, Ministry of Education, School of Physics and Materials Science, East China Normal University, Shanghai 200062, China

^b School of Automation Engineering, Shanghai University of Electric Power, Shanghai 2000902, China

^c Shanghai Key Laboratory of Magnetic Resonance, School of Physics and Materials Science, East China Normal University, Shanghai 200062, China

GRAPHICAL ABSTRACT



ARTICLE INFO

Keywords:

Li doped hierarchical TiO₂
Quasi-scaffold layer
Perovskite solar cells
Conductivity

ABSTRACT

Circular plate like lithium doped hierarchical TiO₂ (Li-hier-TiO₂) nanostructures were synthesized and scattered on the compact TiO₂ layer as a quasi-scaffold layer for perovskite solar cells (PSCs). The quasi-scaffold layer provides superior contact properties with perovskite layer and helps to form the high quality perovskite film with better crystallinity and less pin-holes. Simultaneously, Li-hier-TiO₂ quasi-scaffold compared to pure hier-TiO₂ quasi-scaffold exhibits superior electronic properties due to the reduced trap states together with better electron transport and extraction abilities. PSCs using Li-hier-TiO₂ quasi-scaffold layer to host the CH₃NH₃PbI₃ photoactive layer produce substantially higher PCE of 18.25% with suppressed hysteretic behavior, which is obviously higher than PCE (15.64%) of PSCs using pure hier-TiO₂ quasi-scaffold layer.

1. Introduction

Organolead triiodide perovskite solar cells (PSCs) have been feverishly investigated in recent years and already achieved over 22% of power conversion efficiency (PCE). [1–4]. In a standard PSC configuration, perovskite photoactive layer is normally sandwiched by electron transport layer (ETL) and hole transport layer (HTL) to separate

and collect charge carriers produced in perovskite layer, and both ETL and HTL play important roles to transport and collect carriers, which help to get highly efficient PSCs [5]. Especially, the ETL is crucial for determining the performance of PSCs because the transport distance of electrons in CH₃NH₃PbI₃ perovskite layer is significantly shorter compared to holes [6–9]. Thus, the exploration of the novel materials acted as an ETL for PSCs is always an interesting and important scientific

* Corresponding author.

E-mail address: xhchen@phy.ecnu.edu.cn (X. Chen).

<http://dx.doi.org/10.1016/j.cej.2017.08.045>

Received 2 June 2017; Received in revised form 23 July 2017; Accepted 10 August 2017

Available online 11 August 2017

1385-8947/ © 2017 Elsevier B.V. All rights reserved.

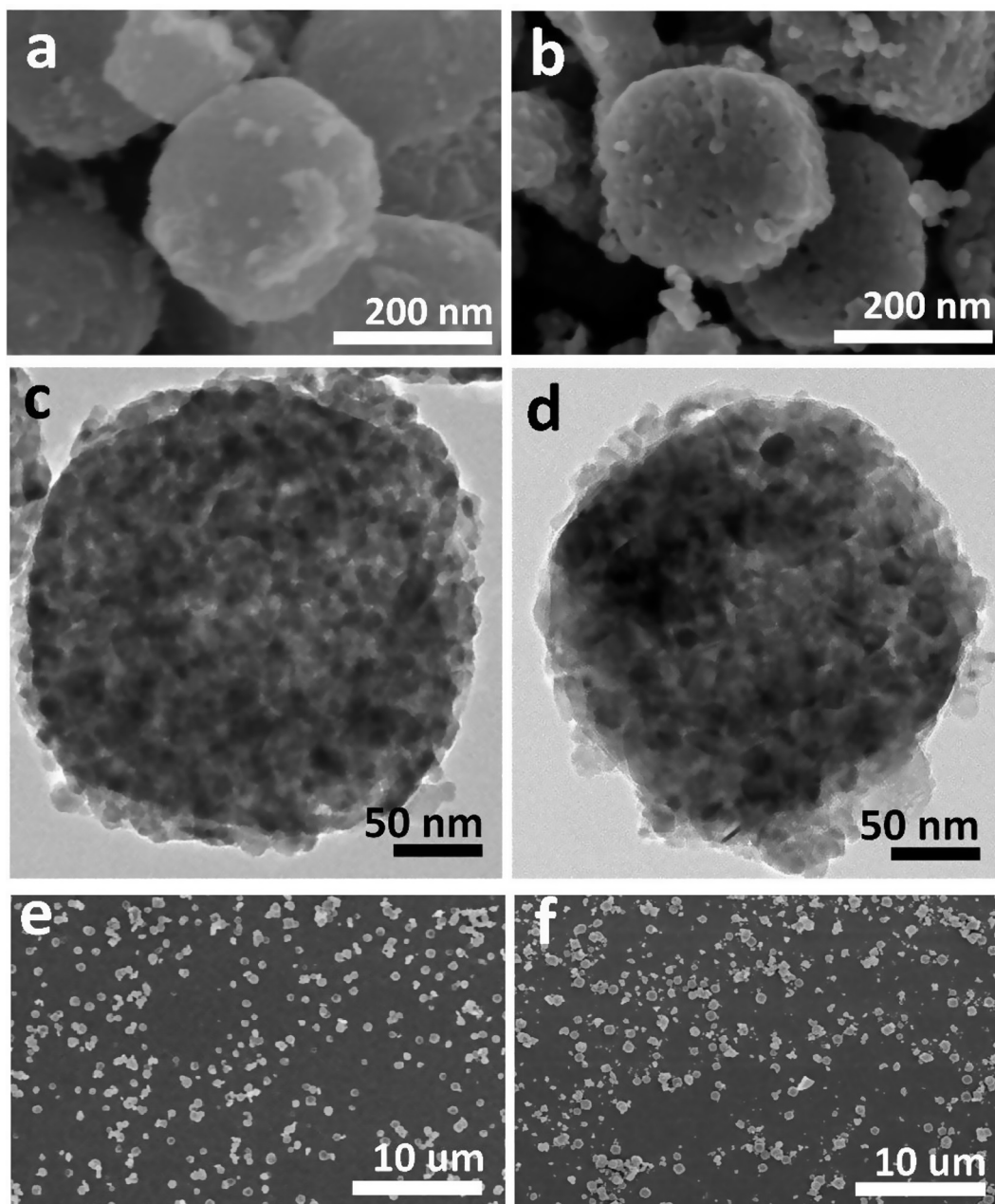


Fig. 1. SEM images of hier-TiO₂ (a) and Li-hier-TiO₂ (b) nanostructures. TEM images of hier-TiO₂ (c) and Li-hier-TiO₂ (d) nanostructures. (e) and (f) are SEM images of quasi-scaffold layer of hier-TiO₂ and Li-hier-TiO₂, respectively.

challenge, including synthetic methodology for an appropriate energy-level alignment along with perovskite layer [10]. Many metal oxides, such as zinc oxide (ZnO) [11,12], tin oxide (SnO₂) [13,14], and titanium dioxide (TiO₂) [15–18] have been applied as ETLs for solar cells. Among these metal oxides, TiO₂ is a good candidate due to the chemical stability, low cost, and the matched band energy level with organo-lead triiodide perovskite layer. Moreover, the morphology of TiO₂ can be easily tailored by synthesis approaches to benefit the perovskite grains growth and carrier transport [19–22]. A competent morphology of TiO₂ scaffold layer not only can improve the carrier transport ability, but also can change the growth kinetics of perovskite grains to form high quality perovskite films with less defects and improve the interface contact properties [23–25]. The conventional mesoscopic scaffold layer prepared by small size TiO₂ nanoparticles (npt-TiO₂) usually forms a labyrinthine structure with tiny space, which limits perovskite grains growth inside TiO₂ scaffold and easily forms lots of voids, leading to

increase carrier recombination and leakage currents of PSCs. Therefore, a capacious scaffold is expected to grow high quality perovskite film with large grain size and less pin-holes. Yu et al. used a three-dimensional (3D) TiO₂ nanowire architecture instead of conventional nanoparticle system, which improves the contact characteristic at the interface of perovskite/TiO₂, and shows an excellent charge transport ability [23]. Yang et al. employed 100 nm size spherical TiO₂ aggregates as scaffold layer for PSCs and obtained an over 18% PCE, which is obviously higher than those PSCs with small size npt-TiO₂ as scaffold [26]. The enhanced efficiency of PSCs is attributed to the large growth spaces inside scaffold helps to form high quality of perovskite layer with large grain size and less pin-holes. In our previous work, porous circular plate-like hierarchical TiO₂ (hier-TiO₂) nanostructures sintered from MIL-125(Ti) MOFs were acted as scaffold of scattered distribution to form a quasi-mesoscopic perovskite solar cells (QM-PSCs) [27]. The hier-TiO₂ quasi-mesoscopic scaffold shows superior

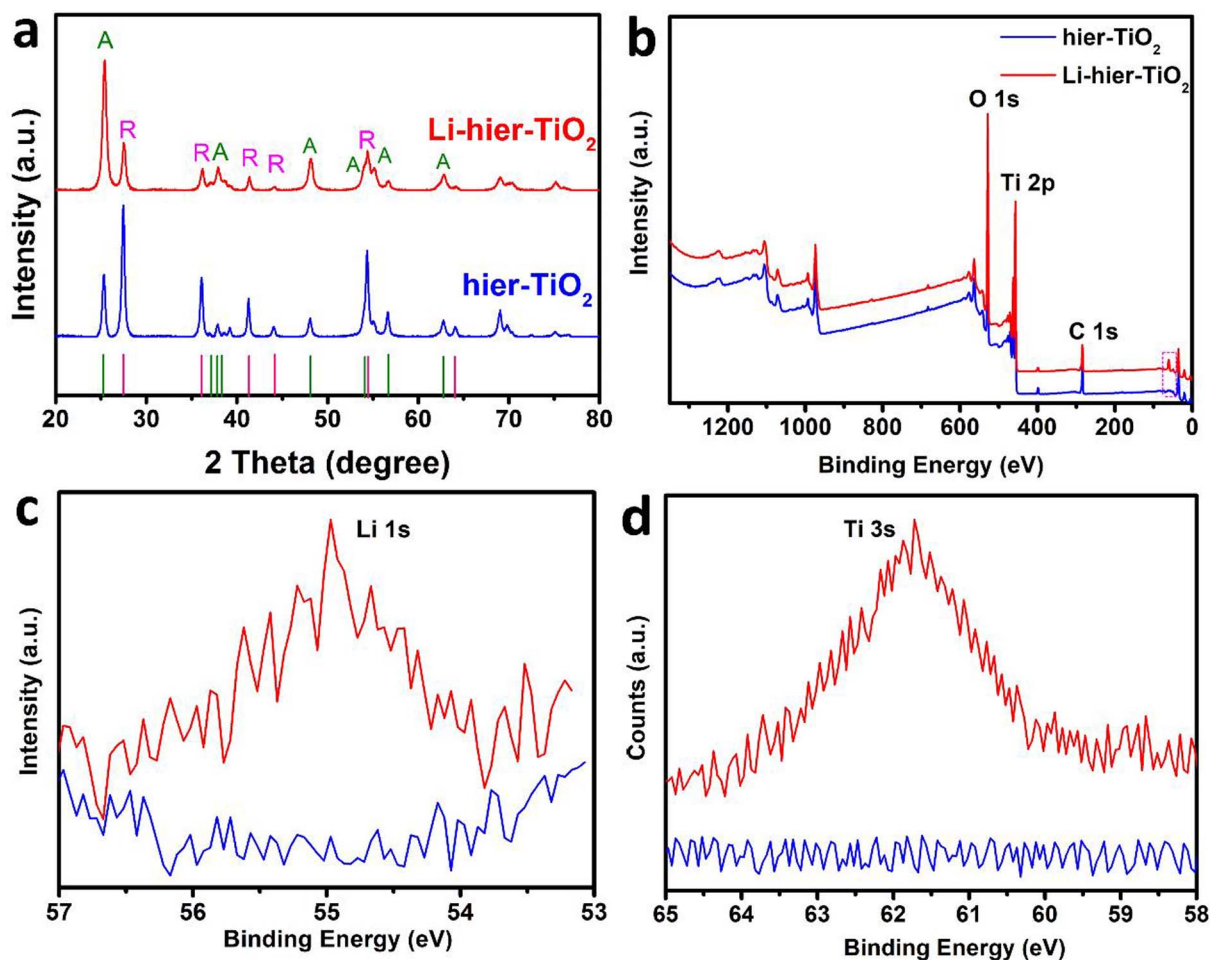


Fig. 2. (a) XRD patterns, (b) XPS spectra of hier-TiO₂ and Li-hier-TiO₂ nanostructures. (c) and (d) are the corresponding Li 1 s and Ti 3 s narrow XPS spectra, respectively.

wettability and offers enough large spaces to grow high quality perovskite layer with large grain size and less pin-holes. Besides, this hier-TiO₂ quasi-mesoscopic scaffold can enhance the light scattering to improve the incident light use ratio. As a result, PSCs based on hier-TiO₂ quasi-mesoscopic scaffold show a PCE of 16.56%, which is obviously higher than PCE (11.38%) of PSCs with conventional TiO₂ nanoparticles (npt-TiO₂) as scaffold.

However, the inferior electron mobility of TiO₂ usually limits the transportation and extraction of photo-generated electrons from perovskite layer. Furthermore, the defects of TiO₂ would trap the carriers and increase carrier recombination [28,29]. Doping or mixing some elements in TiO₂ has been demonstrated a good strategy to inhibit defects and improve the electron transport ability [30–33]. For instance, Zhou et al. used Y-doped TiO₂ as ETL in PSCs and got a high PCE of 19.3% [5]. Nb [34], Mg [35], Al [33] and many other elements doped TiO₂ are used as ETL of PSCs, which can greatly improve PCEs. Noticeably, J. H. Heo et al. reported that the charge carrier mobility of mesoscopic TiO₂ scaffold layer can increase from $1.1 \times 10^{-6} \text{ cm}^2/\text{V s}$ to $2.5 \times 10^{-6} \text{ cm}^2/\text{V s}$ through Li (Lithium) treatment and the corresponding PSCs significantly reduced the J-V hysteresis [36]. Similarly, F. Giordano et al. improved the PCE of PSCs from 17% to over 19% with negligible hysteretic behavior by doping Li into mesoporous TiO₂ scaffold layer [16]. The enhanced photovoltaic performance is attributed to the increase of the conductivity and passivation effect due to doping Li ions.

Herein, the reported hier-TiO₂ nanostructures were further doped with Li ions to form Li doped hierarchical TiO₂ nanostructures (Li-hier-TiO₂), which overcame the disadvantage of the inferior conductivity of hier-TiO₂ nanostructures. The Li-hier-TiO₂ quasi-mesoscopic scaffold

still remains the advantages of pure hier-TiO₂ quasi-mesoscopic scaffold to grow high quality perovskite films, and Li doping further improves electron transport and extraction ability. PSCs using Li-hier-TiO₂ quasi-mesoscopic scaffold show a PCE of 18.25% with less J-V hysteresis, which is much higher than PCE (15.64%) of PSCs using hier-TiO₂ as quasi-mesoscopic scaffold.

2. Experimental

2.1. Materials

All solvents and reagents were used as received. Fluorine-doped tin oxide (FTO) glass (thickness: 2.2 mm, sheet resistance: $14 \Omega \square^{-1}$) were purchased from Nippon Sheet Glass, Japan. Tetra-n-butyl titanate Ti (OC₄H₉)₄, anhydrous methanol, and anhydrous ethanol were purchased from Sinopharm Chemical Reagent Co., Ltd., China. Terephthalic acid (TPA), dimethylformamide (DMF), dimethyl sulfoxide (DMSO), Lithium bis(trifluoromethanesulfonyl)imide (Li-TFSI, 98%) and 4-tert-butylpyridine (TBP, 98%) were purchased from Aladdin company (Shanghai, China). Lead (II) iodide (PbI₂, 99.999%) and ethyl cellulose were purchased from Sigma-Aldrich. CH₃NH₃I (MAI) was purchased from 1-Material-Organic Nano Electronic (1-Material Inc.). 2,2',7,7'-tetrakis (N,N-di-p-methoxy-phenylamine)-9,9'-spirobifluorene (Spiro-OMeTAD, $\geq 99\%$) was purchased from Polymer Light Technology Corp. (Xi'an, China).

2.2. Preparation of Li-hier-TiO₂ pastes

Porous circular plate-like Li-hier-TiO₂ was prepared by sintering

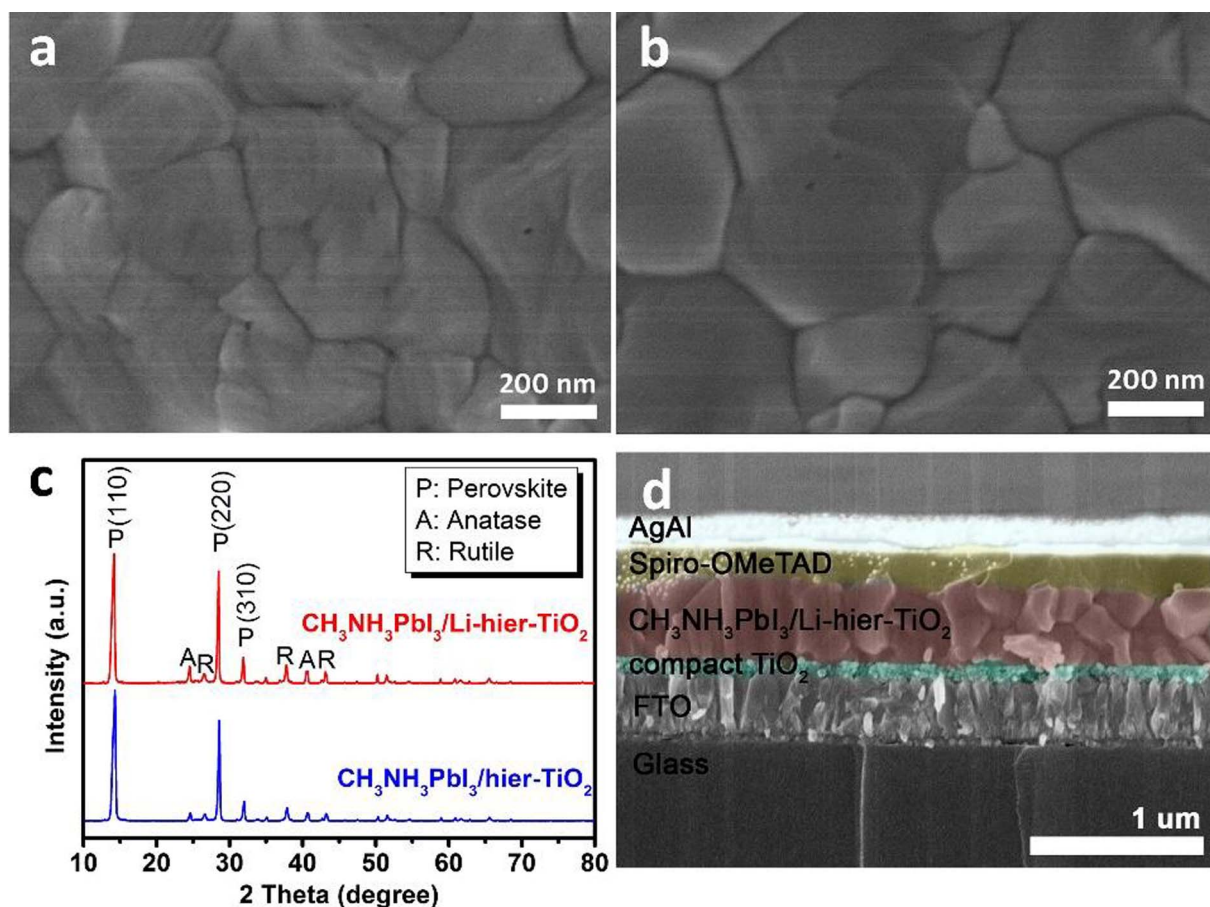


Fig. 3. Top-view SEM images of perovskite layer located on (a) hier-TiO₂ and (b) Li-hier-TiO₂ scaffold. (c) XRD patterns of CH₃NH₃PbI₃/hier-TiO₂ and CH₃NH₃PbI₃/Li-hier-TiO₂. (d) Cross-section SEM image of PSCs using Li-hier-TiO₂ as quasi-scaffold layer.

Li-MIL-125(Ti) MOFs in air. The Li-MIL-125(Ti) MOFs was synthesized by modifying the procedure reported elsewhere [37]. Specifically, different amount Li-TFSI (0.75 g, 1 g, 1.25 g and 1.5 g) were respectively added into four autoclaves with Teflon cup each containing the mixture of 3.0 g TPA, 6 ml anhydrous methanol, 1.56 ml Ti(OC₄H₉)₄ and 54 ml DMF, then heated at 120 °C for 20 h, respectively. Upon cooling down, the white suspensions were centrifuged at 4000 rpm for 10 min and washed with anhydrous methanol several times to get the Li-MIL-125(Ti) MOFs. The MOFs were dried in vacuum oven overnight at 60 °C to completely evaporate the DMF and then sintered at 500 °C for 5 h to convert into porous Li-hier-TiO₂ nanostructures. The corresponding products were named as 0.75 Li-hier-TiO₂, 1 Li-hier-TiO₂, 1.25 Li-hier-TiO₂ and 1.5 Li-hier-TiO₂, respectively.

0.1 g of as prepared Li-hier-TiO₂ were dispersed in 2 ml absolute ethanol solvent by sonication and stirring for 2 h, then 0.5 ml α -terpinol and 0.05 g ethyl cellulose were added to the suspension to increase the viscosity. Finally the resultant solution was sonicated for 30 min and stirred overnight.

For comparison, un-doped hier-TiO₂ paste was prepared under the same condition except that Li-TFSI was not introduced into the reacting system. The detail procedure was reported in our previous work [27].

2.3. Fabrication of PSCs

The patterned FTO substrates were ultrasonically cleaned using deionized water, acetone and isopropanol, then treated under UV-ozone for 15 min. A compact TiO₂ layer with 40 nm thickness was spin-coated on FTO substrate and sintered at 500 °C for 30 min. The Li-hier-TiO₂ slurry was spin-coated onto compact TiO₂ layer and then heated at 500 °C for 30 min. Finally, the samples were immersed in 40 mM TiCl₄

aqueous solutions for 30 min at 70 °C and washed with deionized water and ethanol, followed by annealing at 500 °C for 30 min in air.

The perovskite layer was spin-coated on the TiO₂ layer via a solvent-modified engineering assisted with one-step spin-coating procedure. Specifically, pre-mixed solution containing 159 mg CH₃NH₃I, 462 mg PbI₂, 78 mg DMSO and 600 mg DMF were dropped on the substrate and then the substrate was spun at 4000 rpm for 40 s. Within the first 6 s of spinning, 0.5 mL anhydrous diethyl ether was continuously dropped on the substrate. Then, the substrates were heated at 100 °C for 10 min. After cooling to room temperature, 72.3 mg Spiro-OMeTAD, 28.8 μ l TBP and 17.5 μ l Li-TFSI in acetonitrile (520 mg ml⁻¹) mixture solution were dissolved in 1 ml chlorobenzene and then spin-coated onto the perovskite layer to form a 60 nm thick hole transport layer. Finally, a 80 nm thick AgAl alloy electrode was thermally evaporated onto HTL to form the back contact of the device.

2.4. Characterization

The morphology, structure and composition of samples were investigated by field-emission scanning electron microscopy (FESEM, Hitachi S-4800), transmission electron microscopy (TEM, JEM-2100), X-ray diffraction (XRD, Holland Panalytical PRO PW3040/60) with Cu K α radiation ($V = 30$ kV, $I = 25$ mA). The photocurrent density-voltage (J-V) curve was measured using a Keithley model 2440 Source Meter under the illumination of AM 1.5 G and 100 mW/cm² simulated solar light from a Newport solar simulator system. During the photovoltaic measurements, all devices were masked with a mask to define the active area of 0.10 cm². The incident photon to current conversion efficiency (IPCE) was measured using a Newport Optical Power Meter 2936-R controlled by TracQ Basic software.

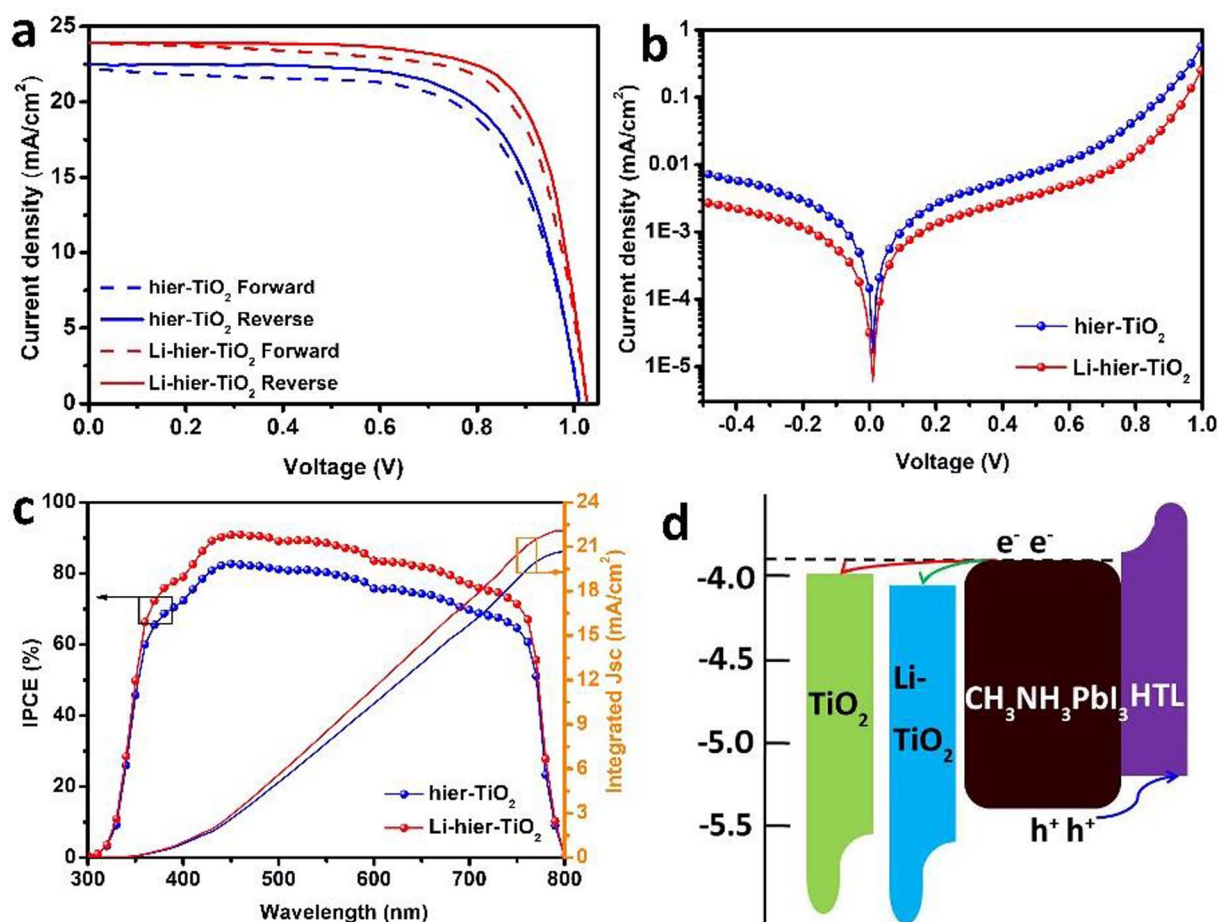


Fig. 4. (a) J-V curves of PSCs based on hier-TiO₂ and Li-hier-TiO₂ scaffold scanned with forward and reverse directions. (b) Dark J-V curves of hier-TiO₂ and Li-hier-TiO₂ based PSCs. (c) IPCE spectra and corresponding integrated current densities of PSCs with hier-TiO₂ and Li-hier-TiO₂ scaffold. (d) Diagram of energy levels (relative to the vacuum level) of each functional layer of cells.

Table 1
Photovoltaic parameters of best PSCs based on hier-TiO₂ and Li-hier-TiO₂.

devices	Scan direction	V _{oc} (V)	J _{sc} (mA/cm ²)	FF (%)	PCE (%)
hier-TiO ₂	Forward	1.01	22.19	66.05	14.80
	Reverse	1.01	22.46	68.93	15.64
Li-hier-TiO ₂	Forward	1.03	23.85	72.06	17.70
	Reverse	1.03	23.91	74.11	18.25

3. Results and discussion

Fig. 1a and b show the SEM images of synthesized hier-TiO₂ and Li-hier-TiO₂ nanostructures, respectively. Both hier-TiO₂ and Li-hier-TiO₂ nanostructures present circular plate-like morphologies with the sizes of about 200–300 nm. This indicates that the topography of hier-TiO₂ nanostructures is not changed by doping Li element. However, the surface of Li-hier-TiO₂ nanostructures shows more abundant pores, which can further improve the capillary effect and wettability benefiting perovskite fully infiltration. Fig. 1c and d present TEM images of hier-TiO₂ and Li-hier-TiO₂ nanostructures, respectively. The observed abundant pores indicate that both types of nanostructures are partly inherited the porosity of MIL-125(Ti). The specific surface areas of hier-TiO₂ and Li-hier-TiO₂ were measured with Brunauer-Emmett-Teller (BET) and show 87.36 m² g⁻¹ and 96.12 m² g⁻¹, the corresponding pore size distribution were calculated by the Barrett-Joyner-Halenda (BJH) method and the main pore sizes are about 8 nm and 11 nm respectively, as shown in Fig. S1a and b. In comparison to TiO₂

nanoparticles (18-NRT) with 42.35 m² g⁻¹ surface area and 6 nm pore size, perovskite precursor solution is more possibly infiltrated into the pores of hier-TiO₂ and Li-hier-TiO₂ nanostructures due to the stronger capillary effect and larger pore sizes, which help to tightly anchor perovskite grains and improve grains stability [27]. Fig. 1e and f show the top view SEM images of hier-TiO₂ and Li-hier-TiO₂ scattered on the compact TiO₂ layer to form a quasi-scaffold layer with scattered distribution, respectively. This quasi-scaffold layer can offer enough spaces to grow perovskite grains.

The structure and composition of hier-TiO₂ and Li-hier-TiO₂ nanostructures were also studied. Fig. 2a shows the XRD patterns of hier-TiO₂ and Li-hier-TiO₂. The hier-TiO₂ and Li-hier-TiO₂ show the mixed crystal structures of anatase and rutile according to JCPDS 21-1272 and JCPDS 21-1276. However, the ratio of anatase to rutile for Li-hier-TiO₂ nanostructures is obviously higher than that of hier-TiO₂, indicating that doping Li element can inhibit the phase transformation from anatase to rutile, which is mainly caused by the presence of foreign ions in the crystal lattice [38]. Fig. 2b depicts the XPS spectra of hier-TiO₂ and Li-hier-TiO₂. There are no traces of sulphur or fluorine from the Li-TFSI precursor in Li-hier-TiO₂ sample, indicating that organic group of TFSI sintered at 500 °C were completely removed. The peak at 55 eV of Li 1s spectrum was detected in Li-hier-TiO₂ sample, as shown in the magnification of Fig. 2c, indicating the successful Li doping. A more pronounced shoulder at the higher binding energy side of O1s main peak can be observed in Li-hier-TiO₂, as shown in Fig. S2a, which is consistent with the previous reports of other groups [10,16,39] and is attributed to the formation of interstitial Li ions. There is no obvious difference between Ti 2p spectra of hier-TiO₂ and Li-hier-TiO₂ samples,

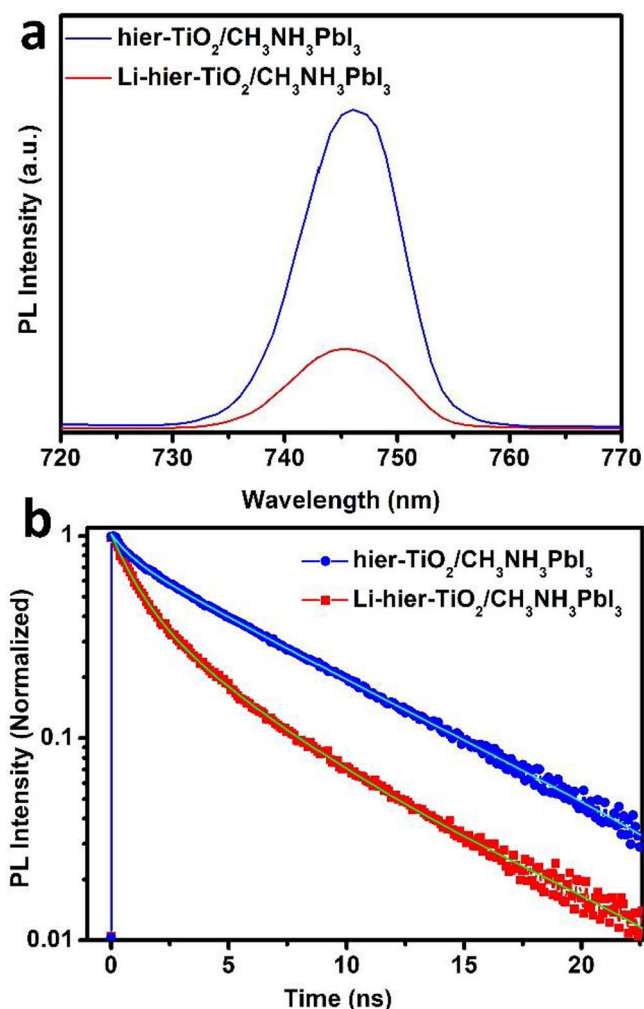


Fig. 5. Steady PL spectra (a) and Time-resolved PL decays (b) of hier-TiO₂/CH₃NH₃PbI₃ and Li-hier-TiO₂/CH₃NH₃PbI₃.

shown in Fig. S2b. The peak at 61.5 eV of Ti 3s shown in Fig. 2d can be ascribed to the presence of Ti³⁺ for Li-hier-TiO₂, indicating that the Li⁺ treatment induces a partial reduction of Ti⁴⁺ to Ti³⁺ within the TiO₂ lattice [40]. The reduction of Ti⁴⁺ to Ti³⁺ can passivate the electronic defects or trap states that originate from oxygen vacancies within the TiO₂ lattice [30], resulting in the improved charge transport property. The band-gaps of hier-TiO₂ and Li-hier-TiO₂ calculated from the UV–vis absorption spectra are 3.38 eV and 3.12 eV respectively, as illustrated in Fig. S3. The bandgap of hier-TiO₂ was slightly reduced after doping Li element, which is attributed to the slightly decreased conduction band of hier-TiO₂ according to the previous reports of Li doping TiO₂ [10,36]. The slightly decreased conduction band of Li-hier-TiO₂ promotes electron injection from perovskite layer to Li-hier-TiO₂ scaffold, which can reduce electron accumulation at the interface of perovskite/TiO₂.

CH₃NH₃PbI₃ layer was prepared by typical one-step method. Fig. 3a and b show top-view SEM images of CH₃NH₃PbI₃ layer located on the quasi-scaffolds of hier-TiO₂ and Li-hier-TiO₂ nanostructures, respectively. The perovskite solar cells fabricated with scaffold of scattered distribution are named as quasi-mesoscopic perovskite solar cells (QM-PSCs) to distinguish the conventional mesoscopic PSCs [27]. The morphologies of CH₃NH₃PbI₃ located on hier-TiO₂ and Li-hier-TiO₂ scaffold are similar and the grain sizes are about 400–1000 nm. Fig. 3c shows the XRD patterns of CH₃NH₃PbI₃ films on hier-TiO₂ and Li-hier-TiO₂ scaffolds, respectively. The strong peaks at 14.08°, 28.41° and 31.85° are assigned to (1 1 0), (2 2 0) and (3 1 0) planes of CH₃NH₃PbI₃,

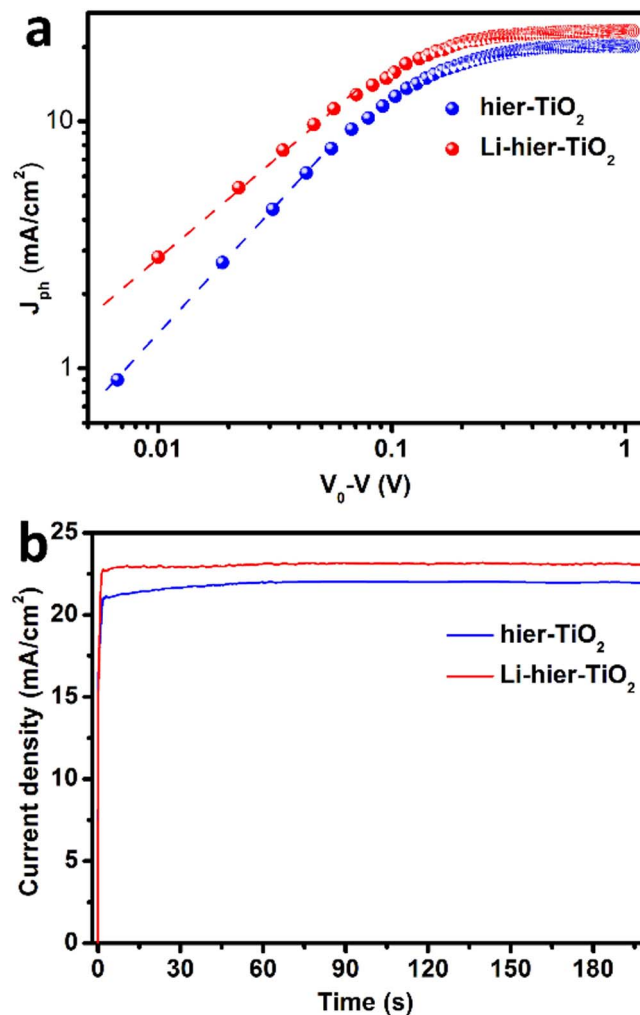


Fig. 6. (a) J_{ph} - V_{eff} plots with double logarithmic axis for PSCs based on hier-TiO₂ and Li-hier-TiO₂ respectively. (b) Time profiles of photocurrent density obtained by holding solar cells at bias voltage of 0.80 V.

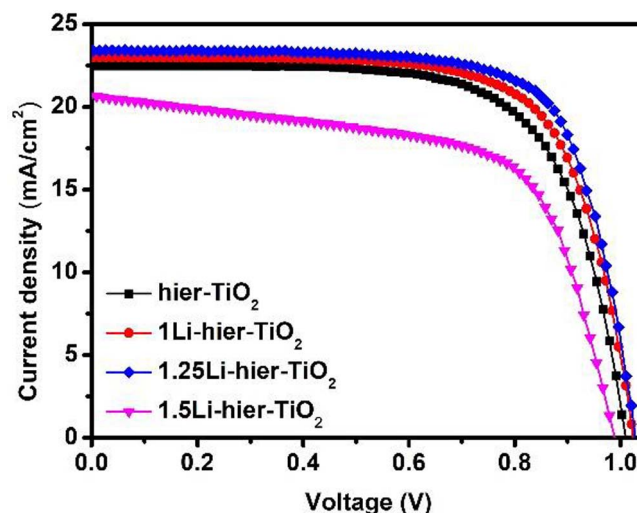


Fig. 7. J–V curves of PSCs based on hier-TiO₂ doped with different Li⁺ concentration.

indicating an orthorhombic crystal structure of halide perovskite with high crystallinity [41,42]. The similar morphologies and XRD patterns of perovskite layer on hier-TiO₂ and Li-hier-TiO₂ scaffolds indicate that doping Li element in hier-TiO₂ nanostructures did not obviously affect

Table 2
Photovoltaic parameters of PSCs based on Li-hier-TiO₂ doped with different Li⁺ concentration.

devices	V _{oc} (V)	J _{sc} (mA/cm ²)	FF (%)	PCE (%)
hier-TiO ₂	1.01	22.46	68.93	15.64
1Li-hier-TiO ₂	1.02	23.02	71.29	16.72
1.25Li-hier-TiO ₂	1.03	23.91	74.11	18.25
1.5Li-hier-TiO ₂	0.99	20.67	63.70	13.03

the crystallization of perovskite layer. Fig. 3d and Fig. S5 present the cross section SEM images of Li-hier-TiO₂ and hier-TiO₂ based PSCs, respectively. Both hier-TiO₂ and Li-hier-TiO₂ quasi-scaffold layer are completely held by CH₃NH₃PbI₃. However, the CH₃NH₃PbI₃ layer located on conventional mesoscopic scaffold with npt-TiO₂ (18-NRT) shows lots of unfilled pinholes, as shown in Fig. S4, indicating that the scattered scaffold has better advantage to grow high quality perovskite films with less pinholes.

Fig. 4a shows the J-V characteristics of best PSCs using hier-TiO₂ and Li-hier-TiO₂ scaffolds and the parameters of cells are listed in Table 1. The short-circuit photocurrent density (J_{sc}), open circuit voltage (V_{oc}) and fill factor (FF) of PSCs using Li-hier-TiO₂ scaffold are higher than those of PSCs with hier-TiO₂ scaffold. Specifically, the J_{sc} of cells was significantly increased from 22.46 to 23.91 mA/cm² for reverse scan and 22.19–23.85 mA/cm² for forward scan after doping Li element. Correspondingly, the FF was increased from 68.93% to 74.11% for reverse scan and 66.05% to 72.06% for forward scan. As a consequence, the cells based on hier-TiO₂ show a PCE of 15.64% for reverse scan and 14.80% for forward scan, while the cells based on Li-hier-TiO₂ show a higher PCE of 18.25% and 17.70% for reverse and forward scan, respectively. The hysteresis difference of J-V curves for PSCs based on Li-hier-TiO₂ between backward and forward scans is 3.0%, which is lower than hysteresis difference (5.4%) of PSCs with hier-TiO₂ because of the suppressed traps and enhanced charge transport capability of Li-hier-TiO₂. PSCs with Li-hier-TiO₂ scattered onto Li doped compact TiO₂ layer can further increase the performance and got the highest PCE of 18.41%, as shown in Fig. S6 and Table S1. This suggested that a dual Li doped TiO₂ ETL helps to further improve electron transport and extraction abilities.

The enhanced performance of Li-hier-TiO₂ based PSCs is further supported by the dark J-V characteristics, as shown in Fig. 4b. The obviously lower reversed saturation current and higher rectification ratio of Li-hier-TiO₂ based PSCs compared to hier-TiO₂ based PSCs demonstrated the reduced carrier recombination and the enhanced carrier transporting and collecting abilities. The reduced leakage current and carrier recombination current can contribute to improving the

Table 3
Photovoltaic parameters of PSCs with quasi-scaffold fabricated with different spin-speed.

Spin speed (rpm.)	sample	V _{oc} (V)	J _{sc} (mA/cm ²)	FF (%)	PCE (%)
1500	hier-TiO ₂	0.99	21.72	53.12	11.46
	Li-hier-TiO ₂	1.02	22.47	58.42	13.26
2000	hier-TiO ₂	1.01	22.46	68.93	15.64
	Li-hier-TiO ₂	1.03	23.91	74.11	18.25
2500	hier-TiO ₂	1.01	22.03	63.19	14.05
	Li-hier-TiO ₂	1.03	23.40	72.78	17.54
3000	hier-TiO ₂	0.99	18.35	58.29	10.60
	Li-hier-TiO ₂	1.00	22.86	70.21	16.05

FF and V_{oc} of cells [27,43], which is consistent with the enhanced FF and V_{oc} for Li-hier-TiO₂ based PSCs. The maximum IPCE values of PSCs based on hier-TiO₂ and Li-hier-TiO₂ are 82.36% and 91.45% and their integrated current density of IPCE spectra are 21.09 mA/cm² and 22.95 mA/cm², respectively, as shown in Fig. 4c, which is consistent with the enhanced J_{sc} of cells doped with Li element.

To test the repeatability of PSCs, we fabricated more than 32 devices in each kind of cells. The statistic PCEs histograms of PSCs based on hier-TiO₂ and Li-hier-TiO₂ are shown in Fig. S7. The relative narrow distribution of PCEs reveals good reproducibility of PSCs and the average PCEs of hier-TiO₂ and Li-hier-TiO₂ are about 15.42% and 17.36% respectively, indicating that Li doped hier-TiO₂ as quasi-scaffold has obvious advantage for improving PCE of quasi-mesoscopic PSCs.

The steady photoluminescence (PL) intensity of CH₃NH₃PbI₃/Li-hier-TiO₂ is much lower than that of CH₃NH₃PbI₃/hier-TiO₂, as shown in Fig. 5a, suggesting that Li-hier-TiO₂ scaffold has better electron transport and extraction ability. Time-resolved PL (TR-PL) decays for CH₃NH₃PbI₃/hier-TiO₂ and CH₃NH₃PbI₃/Li-hier-TiO₂ samples are shown in Fig. 5b. The TR-PL spectra were fitted by a tri-exponential function written as:

$$PL \text{ intensity} = A_1 \exp(-t/\tau_1) + A_2 \exp(-t/\tau_2) + A_3 \exp(-t/\tau_3)$$

where A_1 , A_2 , and A_3 are time independent coefficients of amplitude fraction for each decay component and τ_1 , τ_2 , and τ_3 are decay time of fast, intermediate, and slow component, respectively. The fitted parameters are summarized in Table S1. The amplitude average decay time ($\tau_{amp \text{ avg}} = \frac{\sum A_i \tau_i}{\sum A_i}$) of Li-hier-TiO₂ and hier-TiO₂ based sample were 2.73 ns and 8.20 ns, respectively. The quick attenuation of TR-PL spectrum for CH₃NH₃PbI₃/Li-hier-TiO₂ further confirms that Li-hier-TiO₂ scaffold can more efficiently dissociate excitons and transfer carriers.

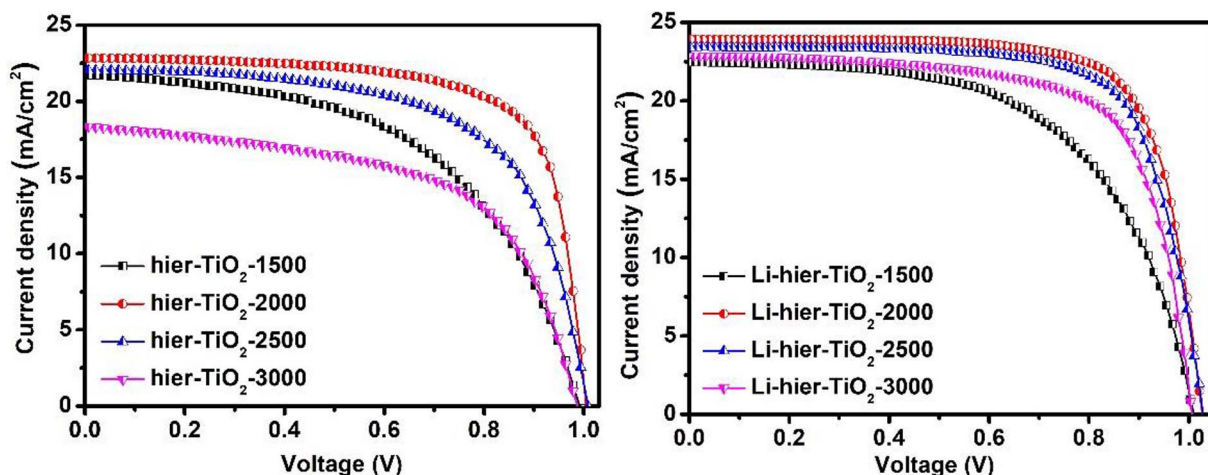


Fig. 8. J-V curves of PSCs using (a) hier-TiO₂ and (b) Li-hier-TiO₂ as scaffold layer fabricated with spin-coated rates of 1500, 2000, 2500 and 3000 rpm, respectively.

To further understand the mechanism responsible for the enhanced performance of Li-hier-TiO₂, the carrier transport and collection properties of PSCs based on hier-TiO₂ and Li-hier-TiO₂ were investigated, respectively. Fig. 6a shows the photocurrent density (J_{ph}) of two types of PSCs. J_{ph} is determined by the equation $J_{ph} = J_{light} - J_{dark}$, where J_{light} and J_{dark} are current densities measured under 1 sun illumination and in dark condition, respectively. The plot of J_{ph} with respect to the effective voltage ($V_0 - V$), where V_0 is the compensation voltage (defined by the voltage at which $J_{ph} = 0$) [44,45] and V is the applied voltage. Noticeably, in low effective voltage (< 0.3 V), the photocurrents in two cells increase sharply with the increase of effective voltage, and the photocurrents reach gradually a saturated value at the higher effective voltage. From Fig. 6a, PSCs based on Li-hier-TiO₂ compared to hier-TiO₂ exhibit a larger saturated photocurrent (J_{sat}). In general, J_{sat} correlates to the maximum exciton generation rate (G_{max}), exciton dissociation probability, and carrier transporting and collection probability at a high effective voltage region. Generally, G_{max} is mainly governed by the light absorption [46]. Considering the constant of absorbed incident photons for given cell, assuming that all the photo-generated excitons are dissociated into free charge carriers at a high effective voltage region, J_{sat} is then limited by the carrier transport and collection. Therefore, carrier transporting and collecting probabilities at any effective voltage can be directly obtained from the ratio of J_{ph}/J_{sat} . The carrier transporting and collection probabilities of PSCs based on hier-TiO₂ and Li-hier-TiO₂ are 91.27% and 94.83% respectively, indicating that Li doped hier-TiO₂ can greatly improve carrier transport and collection capabilities.

The saturation point of photocurrent of PSCs based on Li-hier-TiO₂ and hier-TiO₂ were also checked because it is related to J-V hysteresis with respect to the scan rate and represents the real efficiency of devices [10,27]. The variation of photocurrent density at maximum power condition with the light soaking time under 1 sun irradiation are shown in Fig. 6b. The current density of PSCs based on hier-TiO₂ and Li-hier-TiO₂ were rapidly saturated at 22.31 and 23.27 mA/cm², respectively. The quick response time of PSCs based on Li-hier-TiO₂ further support the obtained results of the higher J_{sc} and less hysteresis for cells with Li-hier-TiO₂.

The Li-doping concentration of hier-TiO₂ was optimized by adding different weight of Li-TFSI into MIL-125(Ti) MOFs precursor solution. Fig. 7 shows the J-V curves of QM-PSCs with different Li concentration under 1 sun irradiation and the photovoltaic parameters are summarized in Table 2. The PCEs of PSCs are gradually improved with increasing Li-TFSI concentration, and PSCs based on 1.25 Li-hier-TiO₂ shows the highest PCE of 18.25%. However, the PCE of PSCs based on 1.5Li-hier-TiO₂ were quickly deteriorated and even more lower than that of the reference PSCs. This is because the excessive Li-doping concentration can introduce lots of defects, which can act as the recombination centers of carriers [10].

The optimized scaffolds of scattered distribution can be controlled by adjusting spin-speed. Fig. 8 shows J-V curves of PSCs using hier-TiO₂ and Li-hier-TiO₂ as quasi-scaffolds and the corresponding photovoltaic parameters are listed in Table 3. The optimized spin-speed is 2000 rpm for both types of scaffolds and got 15.64% and 18.25% PCEs of PSCs for hier-TiO₂ and Li-hier-TiO₂, respectively. Interestingly, doping Li into hier-TiO₂ can not only enhance the photovoltaic performance but also improve the tolerance of fabricating quasi-mesoporous scaffold, because the PCE difference of cells with Li-hier-TiO₂ scaffold is obviously less than that of cells with hier-TiO₂ under the variance of spin-speed from 2000 rpm to 3000 rpm.

The stability of both kinds of PSCs was also compared, as shown in Fig. S8. PSCs without encapsulation were stored in dry cabinet with a relative humidity (RH) of 30% at room temperature. Both PSCs almost show the same decay tendency and remains about 46% of the initial PCE values aging for 30 days, indicating that PSCs with hier-TiO₂ doped without and with Li element both show good stability of moisture.

4. Conclusion

A quasi-mesoscopic PSCs with Li doped hier-TiO₂ nanostructures as quasi-scaffold layer were investigated. Li-hier-TiO₂ based quasi-scaffold layer remains the advantages of pure hier-TiO₂ quasi-mesoscopic scaffold to grow high quality perovskite films, and further can reduce the carrier recombination and exhibit superior contact properties, and better electron transport and extraction abilities. PSCs with Li-hier-TiO₂ got a PCE of 18.25% with less hysteresis, which is obviously higher than PCE (15.64%) of cells with pure hier-TiO₂. The enhanced PCE and the improved tolerance of PSCs with Li-hier-TiO₂ indicate that Li doped hier-TiO₂ nanostructures as scaffold of scattered distribution is an effective strategy to improve the performance of PSCs, simplify fabrication and reduce the cost of perovskite solar cells.

Acknowledgement

This work was supported by the National Nature Science Foundation of China (61275038 and 11274119).

Appendix A. Supplementary data

Supplementary data associated with this article can be found, in the online version, at <http://dx.doi.org/10.1016/j.cej.2017.08.045>.

References

- [1] Best Research-Cell Efficiencies (NREL, 2016), <https://www.nrel.gov/pv/assets/images/efficiency-chart.png>.
- [2] X. Li, D. Bi, C. Yi, J.-D. Décoppet, J. Luo, S.M. Zakeeruddin, A. Hagfeldt, M. Grätzel, A vacuum flash-assisted solution process for high-efficiency large-area perovskite solar cells, *Science* 353 (2016) 58–62.
- [3] C.-H. Chiang, M.K. Nazeeruddin, M. Grätzel, C.-G. Wu, The synergistic effect of H₂O and DMF towards stable and 20% efficiency inverted perovskite solar cells, *Energy Environ. Sci.* 10 (2017) 808–817.
- [4] M. Grätzel, The light and shade of perovskite solar cells, *Nat. Mater.* 13 (2014) 838–842.
- [5] H. Zhou, Q. Chen, G. Li, S. Luo, T.-B. Song, H.-S. Duan, Z. Hong, J. You, Y. Liu, Y. Yang, Interface engineering of highly efficient perovskite solar cells, *Science* 345 (2014) 542–546.
- [6] H. Liu, Z. Huang, S. Wei, L. Zheng, L. Xiao, Q. Gong, Nano-structured electron transporting materials for perovskite solar cells, *Nanoscale* 8 (2016) 6209–6221.
- [7] Z. Zhu, J. Ma, Z. Wang, C. Mu, Z. Fan, L. Du, Y. Bai, L. Fan, H. Yan, D.L. Phillips, Efficiency enhancement of perovskite solar cells through fast electron extraction: the role of graphene quantum dots, *J. Am. Chem. Soc.* 136 (2014) 3760–3763.
- [8] M. Chen, R.-H. Zha, Z.-Y. Yuan, Q.-S. Jing, Z.-Y. Huang, X.-K. Yang, S.-M. Yang, X.-Hua Zhao, D.-L. Xu, G.-D. Zou, Boron and phosphorus co-doped carbon counter electrode for efficient hole-conductor-free perovskite solar cell, *Chem. Eng. J.* 313 (2017) 791–800.
- [9] X. Huang, Z. Hu, J. Xu, P. Wang, J. Zhang, Y. Zhu, Low-temperature processed ultrathin TiO₂ for efficient planar heterojunction perovskite solar cells, *Electrochim. Acta* 231 (2017) 77–84.
- [10] D. Liu, S. Li, P. Zhang, Y. Wang, R. Zhang, H. Sarvari, F. Wang, J. Wu, Z. Wang, Z.D. Chen, Efficient planar heterojunction perovskite solar cells with Li-doped compact TiO₂ layer, *Nano Energy* 31 (2017) 462–468.
- [11] D. Liu, T.L. Kelly, Perovskite solar cells with a planar heterojunction structure prepared using room-temperature solution processing techniques, *Nat. Photonics* 8 (2014) 133–138.
- [12] M.H. Kumar, N. Yantara, S. Dharani, M. Grätzel, S. Mhaisalkar, P.P. Boix, N. Mathews, Flexible, low-temperature, solution processed ZnO-based perovskite solid state solar cells, *Chem. Commun.* 49 (2013) 11089–11091.
- [13] H.S. Rao, B.X. Chen, W.G. Li, Y.F. Xu, H.Y. Chen, D.B. Kuang, C.Y. Su, Improving the extraction of photogenerated electrons with SnO₂ nanocolloids for efficient planar perovskite solar cells, *Adv. Funct. Mater.* 25 (2015) 7200–7207.
- [14] C. Gao, S. Yuan, B. Cao, J. Yu, SnO₂ nanotube arrays grown via an in situ template-etching strategy for effective and stable perovskite solar cells, *Chem. Eng. J.* 325 (2017) 378–385.
- [15] X. Hou, T. Xuan, H. Sun, X. Chen, H. Li, L. Pan, High-performance perovskite solar cells by incorporating a ZnGa₂O₄: Eu³⁺ nanophosphor in the mesoporous TiO₂ layer, *Sol. Energy Mater. Sol. C* 149 (2016) 121–127.
- [16] F. Giordano, A. Abate, J.P.C. Baena, M. Saliba, T. Matsui, S.H. Im, S.M. Zakeeruddin, M.K. Nazeeruddin, A. Hagfeldt, M. Grätzel, Enhanced electronic properties in mesoporous TiO₂ via lithium doping for high-efficiency perovskite solar cells, *Nat. Commun.* 7 (2016) 10379.
- [17] C. Zhang, Y. Luo, X. Chen, Y. Chen, Z. Sun, S. Huang, Effective improvement of the photovoltaic performance of carbon-based perovskite solar cells by additional solvents, *Nano-Micro Lett.* 8 (2016) 347–357.

- [18] P. Wang, J. Zhang, R. Chen, Z. Zeng, X. Huang, L. Wang, J. Xu, Z. Hu, Y. Zhu, Planar heterojunction perovskite solar cells with TiO₂ scaffold in perovskite film, *Electrochim. Acta* (2017).
- [19] L. Liu, H. Yao, X. Xia, D. Ding, P. Lv, X. Li, J. Wang, B. Zhao, H. Li, X. Liu, A novel dual function acetic acid vapor-assisted thermal annealing process for high-performance TiO₂ nanorods-based perovskite solar cells, *Electrochim. Acta* 222 (2016) 933–937.
- [20] H.-S. Kim, J.-W. Lee, N. Yantara, P.P. Boix, S.A. Kulkarni, S. Mhaisalkar, M. Grätzel, N.-G. Park, High efficiency solid-state sensitized solar cell-based on submicrometer rutile TiO₂ nanorod and CH₃NH₃PbI₃ perovskite sensitizer, *Nano Lett.* 13 (2013) 2412–2417.
- [21] I.S. Yang, J.S. You, S. Do Sung, C.W. Chung, J. Kim, W.I. Lee, Novel spherical TiO₂ aggregates with diameter of 100 nm for efficient mesoscopic perovskite solar cells, *Nano Energy* 20 (2016) 272–282.
- [22] Y. Huang, J. Zhu, Y. Ding, S. Chen, C. Zhang, S. Dai, TiO₂ sub-microsphere film as scaffold layer for efficient perovskite solar cells, *ACS Appl. Mater. Interfaces* 8 (2016) 8162–8167.
- [23] Y. Yu, J. Li, D. Geng, J. Wang, L. Zhang, T.L. Andrew, M.S. Arnold, X. Wang, Development of lead iodide perovskite solar cells using three-dimensional titanium dioxide nanowire architectures, *ACS Nano* 9 (2015) 564–572.
- [24] S.M. Kang, S. Jang, J.K. Lee, J. Yoon, D.E. Yoo, J.W. Lee, M. Choi, N.G. Park, Moth-eye TiO₂ layer for improving light harvesting efficiency in perovskite solar cells, *Small* 12 (2016) 2443–2449.
- [25] S. Jang, J. Yoon, K. Ha, M.-C. Kim, D.H. Kim, S.M. Kim, S.M. Kang, S.J. Park, H.S. Jung, M. Choi, Facile fabrication of three-dimensional TiO₂ structures for highly efficient perovskite solar cells, *Nano Energy* 22 (2016) 499–506.
- [26] I.S. Yang, J.S. You, S.D. Sung, C.W. Chung, J. Kim, W.I. Lee, Novel spherical TiO₂ aggregates with diameter of 100 nm for efficient mesoscopic perovskite solar cells, *Nano Energy* 20 (2016) 272–282.
- [27] X. Hou, L. Pan, S. Huang, W. Ou-Yang, X. Chen, Enhanced efficiency and stability of perovskite solar cells using porous hierarchical TiO₂ nanostructures of scattered distribution as scaffold, *Electrochim. Acta* (2017) 351–358.
- [28] T. Leijtens, G.E. Eperon, S. Pathak, A. Abate, M.M. Lee, H.J. Snaith, Overcoming ultraviolet light instability of sensitized TiO₂ with meso-superstructured organometal tri-halide perovskite solar cells, *Nat. Commun.* 4 (2013) 2885.
- [29] C. Di Valentin, G. Pacchioni, A. Selloni, Reduced and n-type doped TiO₂: nature of Ti³⁺ species, *J. Phys. Chem. C* 113 (2009) 20543–20552.
- [30] A. Zaleska, Doped-TiO₂: a review, *Recent Pat. Eng.* 2 (2008) 157–164.
- [31] F. Fabregat-Santiago, E.M. Barea, J. Bisquert, G.K. Mor, K. Shankar, C.A. Grimes, High carrier density and capacitance in TiO₂ nanotube arrays induced by electrochemical doping, *J. Am. Chem. Soc.* 130 (2008) 11312–11316.
- [32] X. Lü, X. Mou, J. Wu, D. Zhang, L. Zhang, F. Huang, F. Xu, S. Huang, Improved-performance dye-sensitized solar cells using Nb-doped TiO₂ electrodes: efficient electron injection and transfer, *Adv. Fun. Mater.* 20 (2010) 509–515.
- [33] S.K. Pathak, A. Abate, P. Ruckdeschel, B. Roose, K.C. Gödel, Y. Vaynzof, A. Santhala, S.I. Watanabe, D.J. Holliman, N. Noel, Performance and stability enhancement of dye-sensitized and perovskite solar cells by Al doping of TiO₂, *Adv. Fun. Mater.* 24 (2014) 6046–6055.
- [34] X. Yin, Y. Guo, Z. Xue, P. Xu, M. He, B. Liu, Performance enhancement of perovskite-sensitized mesoscopic solar cells using Nb-doped TiO₂ compact layer, *Nano Res.* 8 (2015) 1997.
- [35] J. Wang, M. Qin, H. Tao, W. Ke, Z. Chen, J. Wan, P. Qin, L. Xiong, H. Lei, H. Yu, Performance enhancement of perovskite solar cells with Mg-doped TiO₂ compact film as the hole-blocking layer, *Appl. Phys. Lett.* 106 (2015) 121104.
- [36] J.H. Heo, M.S. You, M.H. Chang, W. Yin, T.K. Ahn, S.-J. Lee, S.-J. Sung, D.H. Kim, S.H. Im, Hysteresis-less mesoscopic CH₃NH₃PbI₃ perovskite hybrid solar cells by introduction of Li-treated TiO₂ electrode, *Nano Energy* 15 (2015) 530–539.
- [37] Y. Fu, D. Sun, Y. Chen, R. Huang, Z. Ding, X. Fu, Z. Li, An amine-functionalized titanium metal-organic framework photocatalyst with visible-light-induced activity for CO₂ reduction, *Angew. Chem.* 124 (2012) 3420–3423.
- [38] C.L. Olson, J. Nelson, M.S. Islam, Defect chemistry, surface structures, and lithium insertion in anatase TiO₂, *J. Phys. Chem. B* 110 (2006) 9995–10001.
- [39] S. Södergren, H. Siegbahn, H. Rensmo, H. Lindström, A. Hagfeldt, S.-E. Lindquist, Lithium intercalation in nanoporous anatase TiO₂ studied with XPS, *J. Phys. Chem. B* 101 (1997) 3087–3090.
- [40] K. Westermark, A. Henningsson, H. Rensmo, S. Södergren, H. Siegbahn, A. Hagfeldt, Determination of the electronic density of states at a nanostructured TiO₂/Ru-dye/electrolyte interface by means of photoelectron spectroscopy, *Chem. Phys.* 285 (2002) 157–165.
- [41] M.M. Tavakoli, L. Gu, Y. Gao, C. Reckmeier, J. He, A.L. Rogach, Y. Yao, Z. Fan, Fabrication of efficient planar perovskite solar cells using a one-step chemical vapor deposition method, *Sci. Rep.* 5 (2015) 14083.
- [42] F. Li, C. Ma, H. Wang, W. Hu, W. Yu, A.D. Sheikh, T. Wu, Ambipolar solution-processed hybrid perovskite phototransistors, *Nat. Commun.* 6 (2015) 8238.
- [43] H. Luo, X. Lin, X. Hou, L. Pan, S. Huang, X. Chen, Efficient and air-stable planar perovskite solar cells formed on graphene-oxide-modified PEDOT: PSS hole transport layer, *Nano-Micro Lett.* 9 (2017) 39.
- [44] X. Jia, Z. Jiang, X. Chen, J. Zhou, L. Pan, F. Zhu, Z. Sun, S. Huang, Highly efficient and air stable inverted polymer solar cells using LiF-modified ITO cathode and MoO₃/AgAl alloy anode, *ACS Appl. Mater. Interfaces* 8 (2016) 3792–3799.
- [45] F.-C. Chen, J.-L. Wu, C.-L. Lee, Y. Hong, C.-H. Kuo, M.H. Huang, Plasmonic-enhanced polymer photovoltaic devices incorporating solution-processable metal nanoparticles, *App. Phys. Lett.* 95 (2009) 182.
- [46] M.-F. Xu, X.-Z. Zhu, X.-B. Shi, J. Liang, Y. Jin, Z.-K. Wang, L.-S. Liao, Plasmon resonance enhanced optical absorption in inverted polymer/fullerene solar cells with metal nanoparticle-doped solution-processable TiO₂ layer, *ACS Appl. Mater. Interfaces* 5 (2013) 2935–2942.